A modified super-twisting sliding mode control for slotless self-bearing motor considering disturbance rejection

Huy Kiet Ngo[1], Dung Anh Vu Tien[1], Van Nam Giap[1] and Quang Dich Nguyen[1,*]

[1]*Hanoi University of Science and Technology*
[*]*Corresponding author E-mail: dich.nguyenquang@hust.edu.vn*
DOI: https://doi.org/10.64032/mca.v30i4.472

Abstract

This paper presents a novel application of a modified super-twisting algorithm (MSTA) sliding mode control (SMC) for both position and rotation control of a slotless self-bearing motor (SSBM). The main contributions of this study are the practical synthesis and validation of the MSTA-SMC, which strategically incorporates proportional and integral actions into the super-twisting structure to accelerate convergence and minimize steady-state errors under continuous physical disturbances. To achieve this, the nonlinear dynamic model of the SSBM is first established, followed by the design of the MSTA control laws and a Lyapunov stability analysis to guarantee finite-time reachability to the sliding manifolds. Finally, simulation and real-time hardware experiments using a dSPACE platform are conducted under various operational conditions, including levitation start-up, speed reversals, and sudden external force and torque injections. To quantify its practical advantages, the proposed method is evaluated against both a standard PID controller and the standard STA. In hardware experiments, MSTA-SMC achieves symmetric speed reversal in 0.70 s, representing a 46.2% reduction relative to standard STA. Furthermore, it limits maximum radial displacement to 0.25 mm under a 1 N force and reduces steady-state current chattering by approximately 20% while ensuring overshoot-free levitation.

Keywords: *Disturbance Effects; Modified Super-Twisting; Sliding Mode Control; Slotless Self-Bearing Motor*

Symbols

Symbols	Units	Description
τ	N·m	Motor torque
F_x	N	x-axis bearing force
F_y	N	y-axis bearing force
i_m	A	Torque current
i_x	A	Bearing force f_x current
i_y	A	Bearing force f_y current
k_{nm} k_m		Torque coefficient
k_{nb} k_b		Bearing force coefficient
l_p	m	Length of parallel segment of 1 winding
l_t	m	Length of serial segment of 1 winding
r	m	Rotor radius
B_0	T	Maximum magnetic flux density in the air gap
α	rad	Rotor angular position
β	rad	Torque current phase angle

Abbreviations

SBM	Self-bearing motor
SSBM	Slotless self-bearing motor
PID	Proportional-Integral-Derivative
SMC	Sliding mode control
STA	Super-Twisting Algorithm
MSTA	Modified Super-Twisting Algorithm

1. Introduction

Self-bearing motors (SBM) have become increasingly vital in advanced electromechanical systems. By integrating magnetic levitation and electromagnetic torque generation within a stator structure, SBMs eliminate the need for physical mechanical bearings. This contactless model offers remarkable advantages, including the elimination of mechanical dissipation and improved power density. Consequently, SBMs are widely utilized for high-speed and high-precision applications, particularly in demanding or sensitive environments where traditional bearings cause rapid degradation [1]. Capitalizing on their levitation capabilities, SBMs have been successfully deployed in various critical fields, ranging from artificial blood pumps and flywheel energy storage systems to ultra-clean room manufacturing equipment [2-4].

Among the diverse SBM topologies, the slotless self-bearing motor (SSBM) has attracted considerable research interest. The notable structural feature of the SSBM is the complete removal of stator teeth, an architectural design that inherently eliminates torque ripple and significantly enhances rotational smoothness [5]. Over the past two decades, hardware optimization for SSBMs has progressed rapidly, enhancing the boundaries of ultra-high-speed operation and overall energy efficiency [6-7]. However, despite these electromechanical advancements, the realization of precise and stable operation remains a control challenge. In practical deployments, SSBMs are inevitably subjected to a spectrum of lumped disturbances, including rotor mass eccentricity, parametric variations, and unpredictable external load torques, all of which

Received: 05 August 2026; Revised: 29 October 2026; Accepted: 29 October 2026.

can severely compromise the levitation stability and speed tracking precision [8].

Historically, early control architectures for SSBMs utilized proportional-integral-derivative (PID) controllers due to their straightforward implementation [9]. While these linear control schemes verified the baseline feasibility of magnetic suspension, they exhibited inherent limitations when dealing with complex nonlinearities. Specifically, linear controllers may exhibit limited dynamic stiffness to actively suppress persistent and severe perturbations, resulting in degraded transient and steady-state performance under varying operational conditions.

To address the limitations of linear regulation, robust nonlinear methodologies, most notably sliding mode control (SMC), have been extensively investigated for controlling these motors [10]. SMC is widely adopted due to its strong robustness against matched uncertainties and parameter variations [11]. Nevertheless, the industrial applicability of conventional first-order SMC is constrained by the chattering phenomenon. The discontinuous high frequency switching actions required to enforce sliding mode behavior can excite unmodeled mechanical resonances, generate acoustic noise, and induce severe thermal losses in the motor windings [12]. Although boundary layer techniques are frequently employed to smooth the control signal, they inherently sacrifice tracking precision, leading to bounded steady-state errors rather than asymptotic convergence.

To preserve the robustness of SMC while reducing chattering, second order sliding mode algorithms, particularly the super-twisting algorithm (STA), have been introduced to SSBM systems. In our recent work [13], a fractional-power STA was implemented on the 3-DOF SSBM prototype to yield a continuous control effort and finite-time convergence to the sliding manifold. However, because the reaching law in [13] relies solely on nonlinear fractional switching gains, it exhibits slow reaching speeds when initial tracking errors are large. Moreover, to inject linear damping into the equivalent control law, the speed loop in [13] required an integral PI-type sliding surface, which introduced double-integration lag and restricted the speed tracking error to asymptotic convergence. A detailed technical comparison distinguishing the present work from [13] is summarized in Table 1 in Section 3.3.

Motivated by the need for enhanced dynamic response and high tracking accuracy without over-amplifying switching gains, this paper proposes a practical and robust control strategy by adapting the modified super-twisting algorithm (MSTA) originally presented in [14]. In [14], the MSTA was combined with an extended state observer (ESO) for the single-axis first-order speed regulation of a conventional 3-phase SPMSM. In this study, we adopt the baseline MSTA reaching law to synthesize an observer-free, multi-axis control framework for the 6-phase 3-DOF SSBM, encompassing both second-order radial levitation subsystems and a first-order rotational speed subsystem. By integrating linear proportional and integral correction terms directly into the super-twisting structure, the proposed MSTA-SMC accelerates the convergence rate under large initial errors, and effectively eliminates steady-state errors under constant disturbances.

The contributions of this paper are as follows:

1. A comprehensive dynamic model of the SSBM is established, explicitly incorporating lumped disturbances to account for system uncertainties and external mechanical impacts across all operational axes.
2. A robust MSTA-SMC framework is designed for both the second-order levitation subsystem and the first-order rotational speed subsystem. The finite-time reachability to the sliding manifolds and closed-loop stability are proven using Lyapunov stability theory.
3. The performance of the proposed controller is validated through numerical simulations and real-time hardware experiments using a dSPACE platform. To highlight its practical advantages, the proposed controller is compared with both a conventional PID controller and the standard STA.

The rest of this paper is structured as follows. Section 2 introduces the mathematical model of the SSBM and the general form of the control law. Section 3 presents the design procedure and stability analysis of the proposed MSTA-based controller. Section 4 provides the simulation and experimental results to validate the controller's effectiveness. Finally, Section 5 concludes the paper and outlines future research directions.

2. Preliminary mathematics and the proposed control law

2.1 Mathematical model

Figure 1 illustrates the structure of the motor, with detailed specifications provided in [9]. The motor consists of two primary components: a rotor and a stator. The rotor features a radially magnetized permanent magnet that utilizes an external iron yoke to establish a closed magnetic circuit. An aluminum clamp secures these two rotor components together. Positioned within the rotor's air gap is the stator, which comprises six-phase coreless windings designated as phases a, b, c, d, e, and f. These six phases are distributed symmetrically along the circular path of the air gap.

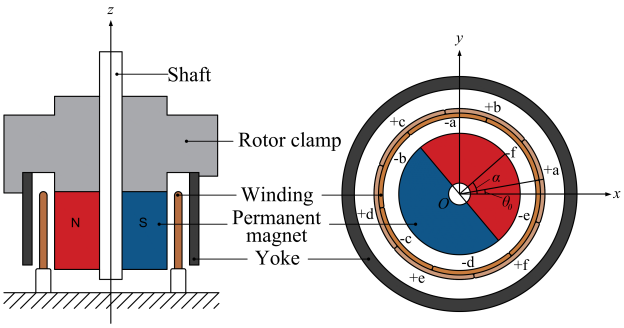


Figure 1: Slotless self-bearing motor structure.

In an ideal working condition without any manufacture errors or external forces, our previous paper [9] has shown that the generated torque τ and the radial bearing forces F_x, F_y are linearly proportional to the control currents:

$$\begin{cases} \tau = k_{nm}\, k_m\, i_m \\ F_x = k_{nb}\, k_b\, i_x \\ F_y = k_{nb}\, k_b\, i_y \end{cases} \tag{1}$$

where i_m, i_x, i_y are currents generating the above torque and forces. The parameters k_{nm}, k_m, k_{nb}, k_b are the nominal force

and torque coefficients determined by the motor's geometry and magnetic flux density and are described as the following equations:

$$\begin{aligned} k_{nm} &= 1+2\cos\left(\frac{\pi}{3n}\right)+2\cos\left(2\frac{\pi}{3n}\right)+\dots \\ &\quad +2\cos\left(\frac{n-1}{2}\frac{\pi}{3n}\right) \\ k_m &= \left(3\sqrt{2}l_p+\frac{8\left(6-3\sqrt{2}\right)}{\pi}l_t\right)rB_0 \\ k_{nb} &= 1+2\cos\left(2\frac{\pi}{3n}\right)+2\cos\left(4\frac{\pi}{3n}\right)+\dots \\ &\quad +2\cos\left((n-1)\frac{\pi}{3n}\right) \\ k_b &= \left(3l_p+\frac{12}{\pi}l_t\right)B_0 \end{aligned} \tag{2}$$

With n is the number of turns each phase; l_p, l_t are the length of winding segment; r is rotor radius; B_0 is the maximum value of the magnetic flux density applied to the coil.

The currents applied to the stator coils are described as:

$$\begin{cases} i_{a,d} = i_x\sin(\alpha)+i_y\cos(\alpha)\pm i_m\cos(\beta) \\ i_{b,e} = i_x\sin\left(\alpha-\frac{2\pi}{3}\right)+i_y\cos\left(\alpha-\frac{2\pi}{3}\right) \\ \pm i_m\cos(\beta+\pi/3) \\ i_{c,f} = i_x\sin\left(\alpha-\frac{4\pi}{3}\right)+i_y\cos\left(\alpha-\frac{4\pi}{3}\right) \\ \pm i_m\cos(\beta+2\pi/3) \end{cases} \tag{3}$$

Herein, α is the angular position of the rotor; β is the angle of the torque current with $\beta=\alpha-\frac{\pi}{4}$.

Based on Newton-Euler equations, the nominal decoupled dynamic equations of the rotor in the translational and rotational axes can be expressed as:

$$\begin{cases} J\dot{\omega} = \tau \\ m\ddot{x} = F_x \\ m\ddot{y} = F_y \end{cases} \tag{4}$$

where J is the moment of inertia, m is the mass, ω is the rotational speed, and x, y are radial position of the rotor.

In practice, the nominal SSBM model in Equations (1)-(4) is subject to both internal parametric uncertainties and external mechanical perturbations, as detailed in [10]. Specifically, fabrication tolerances in the hexagonal coreless winding, including angular placement errors and conductor segment length deviations Δl_p and Δl_t, combine with thermal variations and rotor eccentricity to induce fluctuations in the air-gap flux density ΔB_0 as well as the nominal force and torque coefficients $\Delta k_{nm}, \Delta k_m, \Delta k_{nb}$, and Δk_b. These internal mismatches generate electromagnetic torque and radial force perturbations denoted as $\Delta\tau$, ΔF_x, and ΔF_y. Concurrently, during operation, the rotor experiences an external mechanical load torque T_l and external radial disturbance forces F_{lx} and F_{ly}. Because both internal electromagnetic variations and external mechanical loads act along the same physical degrees of freedom as the control currents, they satisfy the matching condition and can be aggregated into lumped additive disturbances. Consequently, the comprehensive dynamic model of the SSBM is formulated as:

$$\begin{cases} \dot{\omega} = k_\omega i_m + d_\omega(t) \\ \ddot{x} = k_x i_x + d_x(t) \\ \ddot{y} = k_y i_y + d_y(t) \end{cases} \tag{5}$$

where $k_\omega = k_{nm}k_m/J$ and $k_x = k_y = k_{nb}k_b/m$, and the lumped disturbance terms are physically defined as:

$$\begin{cases} d_\omega(t) = \frac{\Delta\tau - T_l}{J} \\ d_x(t) = \frac{\Delta F_x - F_{lx}}{m} \\ d_y(t) = \frac{\Delta F_y - F_{ly}}{m} \end{cases} \tag{6}$$

Assumption 1. The lumped disturbances $d_j(t)$, $j \in x,y,\omega$ are considered unknown but bounded, satisfying $\left|d_j(t)\right| \le \delta_j$, where δ_j denotes the corresponding upper bound of the disturbance.

2.2 Modified super-twisting sliding mode control

In this section, a MSTA reaching law is formulated. While the conventional STA is highly effective against static disturbances, the MSTA introduces additional linear proportional terms to simultaneously enhance the convergence rate and tackle rapidly varying dynamic disturbances.

Let s be considered as the generalized sliding variable for the control system. The switching control signal u_{sw} of the proposed MSTA is defined as follows:

$$u_{sw} = -c_1\mu_1(s) - c_2\int_0^t \mu_2(s)d\tau \tag{7}$$

where

$$\begin{cases} \mu_1(s) = p_1|s|^{\frac{1}{2}}sgn(s)+p_2 s \\ \mu_2(s) = p_1 sgn(s)+p_2 s \end{cases} \tag{8}$$

and c_1, c_2, p_1, and p_2 are positively defined. The fractional-power components $|s|^{\frac{1}{2}}sgn(s)$ and $sgn(s)$ preserve the chattering-compensation property of the original STA. At the same time, the linear terms $p_2 s$ act as an effective proportional feedback mechanism, significantly accelerating the transient response when the initial tracking error is far from the sliding surface.

Upon applying the control law, the closed-loop dynamics of the sliding variable under the lumped disturbance $d(t)$ can be represented as:

$$\begin{cases} \dot{s} = -c_1\mu_1(s)+\varphi \\ \dot{\varphi} = -c_2\mu_2(s)+\dot{d}(t) \end{cases} \tag{9}$$

where φ is an auxiliary state variable representing the integration of the switching law and the external disturbance.

Assumption 2. Assume that the rate of change of the lumped disturbance is bounded such that $\left|\dot{d}(t)\right| \le L_d$ for a positive constant L_d. The generalized sliding variable s will converge to the origin in a finite time if the controller gains are selected as follows:

$$\begin{cases} p_1 > 0 \\ p_2 > 0 \\ c_1 > \frac{L_d}{p_1\sqrt{2(c_2p_1-L_d)}}\left(1+\frac{\gamma_1}{\gamma_2}\right) \\ c_2 > \frac{L_d}{p_1} \end{cases} \tag{10}$$

where $\gamma_1 > \gamma_2 > 0$ are design constants.

Proof. To prove stability, a state vector is defined as $\eta = [\mu_1(s),\ c_1\mu_1(s)-\varphi]^T$. A quadratic Lyapunov function candidate V is chosen as:

$$V = \eta^T R\eta + (\gamma_1+\gamma_2)c_2\left[p_1|s|+\frac{1}{2}p_2 s^2\right] \tag{11}$$

where $\mathbf{R} = \frac{1}{2}\begin{bmatrix} \gamma_1 c_1^2 & -\gamma_1 c_1 \\ -\gamma_1 c_1 & \gamma_1+\gamma_2 \end{bmatrix}$ is a symmetric matrix. Positive definiteness of R follows at once from its leading principal minor $R_{11} = \frac{1}{2}\gamma_1 c_1^2 > 0$ and its determinant $\det R = \frac{1}{4}\gamma_1\gamma_2 c_1^2 > 0$, both of which hold strictly under the standing assumptions $\gamma_1 > 0$, $\gamma_2 > 0$ and $c_1 > 0$. The time derivative of V along the system trajectories is calculated as:

$$\dot{V} = \dot{\eta}^T R\eta + \eta^T R\dot{\eta} + (\gamma_1+\gamma_2)\, c_2\,(p_1 + p_2|s|)\,\dot{s}\; sgn(s) \tag{12}$$

Substituting the dynamics and considering the bound $\left|\dot{d}(t)\right| \le L_d$, the derivative $\dot{V}$ can be expanded and strictly bounded through algebraic calculations as follows:

$$\begin{aligned} \dot{V} \le & -\gamma_2 c_1 \eta_2^2 \left(\frac{p_1}{2\sqrt{|s|}} + p_2\right) - \gamma_1 c_1 \mu_1 \dot{d} \\ & + (\gamma_1+\gamma_2)\,\eta_2 \dot{d} - \gamma_1 c_1 c_2 \mu_1 \mu_2 \\ & + (\gamma_1+\gamma_2)\,\eta_2 c_2 \mu_2 \\ & - (\gamma_1+\gamma_2)\, c_2\,(p_1 + p_2|s|)\,\eta_2\; sgn(s) \end{aligned} \tag{13}$$

By substituting the bounded derivative condition $\left|\dot{d}(t)\right| \le L_d$ from Assumption 2 and applying the gain conditions in (10), the time derivative $\dot{V}$ in (13) can be upper-bounded in a compact quadratic form:

$$\dot{V} \le -\left(\frac{p_1}{2\sqrt{|s|}} + p_2\right)\eta^T Q \eta \tag{14}$$

where Q is a symmetric positive-definite matrix derived from the coefficients of (13). Utilizing the inequality $1/\sqrt{|s|} \ge p_1/\|\eta\|$ and the Rayleigh-Ritz theorem $\lambda_{\min}(Q)\|\eta\|^2 \le \eta^T Q\eta$, one obtains:

$$\dot{V} \le -\frac{p_1^2 \lambda_{\min}(Q)}{2}||\eta|| \tag{15}$$

Furthermore, bounding the Lyapunov function as $V \le \eta^T P\eta \le \lambda_{\max}(P)\|\eta\|^2$, where P is the positive-definite matrix augmenting R with the nonlinear terms of V, yields $\|\eta\| \ge \sqrt{V}/\sqrt{\lambda_{\max}(P)}$. Consequently, the derivative satisfies:

$$\dot{V} \le -\sqrt{k}\sqrt{V} \tag{16}$$

where the positive constant k is explicitly given by:

$$k = \frac{p_1^4 \lambda_{\min}^2(Q)}{4\lambda_{\max}(P)} \tag{17}$$

Based on the comparison principle, the inequality $\dot{V} \le -\sqrt{k}\sqrt{V}$ ensures that V reaches the origin within a finite time $T \le \frac{2\sqrt{V(0)}}{\sqrt{k}}$. Thus, the finite-time convergence of the sliding variable s to the manifold $s = 0$ is guaranteed. □

3. Proposed MSTA-SMC design for the SSBM system

Based on the generalized MSTA presented in Section 2.2, this section details the design of the robust control laws for the radial positions and rotational speed of the SSBM. The primary objective is to achieve precise trajectory tracking and effective rejection of the lumped disturbances, namely $d_x(t)$, $d_y(t)$, and $d_\omega(t)$, ensuring that the rotor is stably levitated at the geometric center while tracking the speed command.

3.1 MSTA-SMC for the x- and y-axes of SSBM system

The primary objective of the radial levitation controller is to regulate the rotor position to the geometric center. Consequently, the proposed controller is designed to enforce finite-time convergence and robustly reject bounded radial disturbances d_x and d_y originating from mechanical unbalances and structural imperfections.

To maintain the rotor at the geometric origin, the control scheme must enforce stable levitation while effectively suppressing radial perturbations d_x and d_y. Considering the second-order dynamics of the translational axes, the sliding surfaces for the x- and y-axes are designed as follows:

$$\begin{cases} s_x = \dot{e}_x + L_b e_x \\ s_y = \dot{e}_y + L_b e_y \end{cases} \tag{18}$$

where $e_x = x - x_{ref}$ and $e_y = y - y_{ref}$ are the position tracking errors, and L_b is a positive constant representing the slope of the linear sliding surface. Taking the time derivative of s_x and substituting the dynamics $\ddot{x} = k_x i_x + d_x(t)$, the error dynamics on the x-axis are expressed as:

$$\dot{s}_x = k_x i_x + d_x(t) - \ddot{x}_{ref} + L_b \dot{e}_x \tag{19}$$

The control current i_x is composed of an equivalent control term i_{xeq} and a switching term i_{xsw}:

$$\begin{cases} i_{xeq} = \frac{1}{k_x}\left(\ddot{x}_{ref} - L_b \dot{e}_x\right) \\ i_{xsw} = -\frac{1}{k_x}\left(c_{b1}\mu_{b1}(s_x) + c_{b2}\int_0^t \mu_{b2}(s_x)\,d\tau\right) \end{cases} \tag{20}$$

where c_{b1} and c_{b2} are the positive control gains for the radial levitation loop, and μ_{b1} and μ_{b2} follow the MSTA structure defined in Section 2.2. Since the sliding surfaces s_x and s_y have the unit of linear velocity m/s, the MSTA parameters must have appropriate physical units. Specifically, p_{b1} is in $(m/s)^{1/2}$, c_{b1} is in $s^{-1/2}$, c_{b2} is in s^{-1}, while p_{b2} is dimensionless.

The total control law for the x-axis is formulated as:

$$i_x = \frac{1}{k_x}\left(\ddot{x}_{ref} - L_b\dot{e}_x - c_{b1}\mu_{b1}(s_x) - c_{b2}\int_0^t \mu_{b2}(s_x)\,d\tau\right) \tag{21}$$

The control current i_y is derived using a symmetric procedure.

3.2 MSTA-SMC for the rotational speed control

The primary objective of the rotational speed controller is to track the reference speed accurately while rejecting the effects of load torque disturbances $d_\omega(t)$. Since the speed dynamics are of the first order, the sliding surface is chosen:

$$s_\omega = e_\omega = \omega - \omega_{ref} \tag{22}$$

The time derivative of the sliding surface, incorporating the dynamics $\dot{\omega} = k_\omega i_m + d_\omega(t)$, yields:

$$\dot{s}_\omega = k_\omega i_m + d_\omega(t) - \dot{\omega}_{ref} \tag{23}$$

Following the MSTA design, the torque current i_m is designed as:

$$i_m = \frac{1}{k_\omega}\left(\dot{\omega}_{ref} - c_{m1}\mu_{m1}(s_\omega) - c_{m2}\int_0^t \mu_{m2}(s_\omega)\,d\tau\right) \tag{24}$$

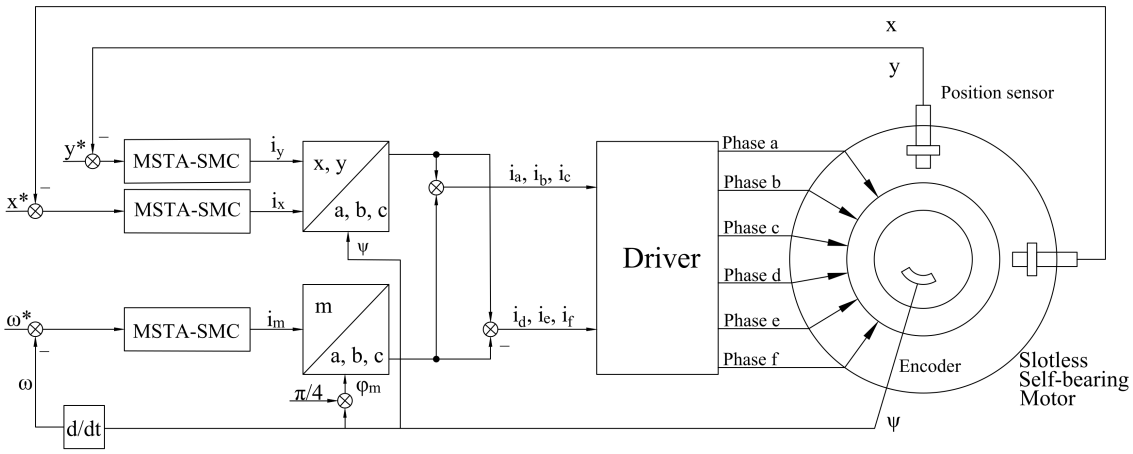


Figure 2: Control structure.

where c_{m1} and c_{m2} are the positive control gains for the speed loop. Similarly, because s_ω has the unit of angular velocity rad/s, the parameters p_{m1}, c_{m1}, and c_{m2} have the corresponding units of $(rad/s)^{1/2}$, $s^{-1/2}$, and s^{-1}, respectively, while p_{m2} is dimensionless.

3.3 Stability analysis

To establish the overall stability of the SSBM system, a composite Lyapunov function is constructed by summing the individual Lyapunov functions associated with each control axis:

$$\mathbf{V}_\Sigma = \mathbf{V}_x + \mathbf{V}_y + \mathbf{V}_\omega \tag{25}$$

where $V_j (j \in \{x, y, \omega\})$ are the quadratic Lyapunov functions discussed in Section 2.2. Assuming the rates of change of the lumped disturbances are bounded by L_{dj}, and the controller gains are tuned to satisfy the stability criteria, the derivative of the total Lyapunov function satisfies:

$$\dot{\mathbf{V}}_\Sigma \leq -\kappa_\Sigma \left(\sqrt{\mathbf{V}_x} + \sqrt{\mathbf{V}_y} + \sqrt{\mathbf{V}_\omega} \right) \leq -\kappa_\Sigma \sqrt{\mathbf{V}_\Sigma} \tag{26}$$

Table 1: Comparison between Ref. [13] and the proposed work.

Criteria	STA-SMC[13]	Proposed MSTA-SMC
Switching law (u_{sw})	$= -k_1 \lvert s \rvert^{\eta_1} \operatorname{sgn}(s) - \int_0^t k_2 \lvert s \rvert^{\eta_2} \operatorname{sgn}(s) d\tau$	$= -c_1 \mu_1(s) - c_2 \int_0^t \mu_2(s) d\tau$
Position surface ($s_{x,y}$)	$= \dot{e}_{x,y} + c_f e_{x,y}$	$= \dot{e}_{x,y} + L_b e_{x,y}$
Speed surface (s_ω)	$= e_\omega + c_\omega \int e_\omega dt$	$= e_\omega$
Stability proof	Homogeneity theory ($V = \chi^T A \chi$)	Strict quadratic Lyapunov ($V = \eta^T R \eta + \ldots$)
Disturbance bound	Bounded magnitude: $\lvert d_j(t) \rvert \leq \delta_j$	Bounded magnitude & derivative: $\lvert d_j(t) \rvert \leq \delta_j$, $\lvert \dot{d}_j(t) \rvert \leq L_{dj}$

This result confirms that the overall system is finite-time stable. The trajectories of the sliding variables converge to their respective sliding manifolds in finite time. Consequently, the speed error achieves finite-time convergence, while the position tracking errors asymptotically stabilize at the origin along the linear sliding manifolds. This ensures high-precision and robust operation of the SSBM.

To highlight the theoretical advancements of the designed control framework, a structural comparison between the previous STA-SMC [13] and the proposed MSTA-SMC is presented in Table 1.

4. Simulation and experiment results

Table 2: Physical and structural specifications of the SSBM.

Parameters	Symbol	Value
Mass of the rotor	m	0.4 kg
Outer radius of the permanent magnet	r_m	0.02 m
Inner radius of the rotor yoke	r	0.025 m
Outer radius of the stator framework	R	0.022 m
Peak air-gap magnetic flux density	B_0	0.59 T
Total turns per stator coil	n	55
Conductor wire diameter	d	0.0008 m
Length of parallel conductor part	l_p	0.008 m
Length of serial conductor part	l_t	0.006 m
Total rotational inertia	J	9.68×10^{-5} kg.m^2

This section evaluates the proposed MSTA-SMC scheme through numerical simulations and real-time experiments. The performance is validated against a well-tuned PID controller and the standard STA. Table 2 lists the motor parameters, and Figure 2 shows the control structure. The experiments use a dSPACE MicroAutoBox III platform.

Control current saturation limits of ± 2 A for rotation and ± 3 A for levitation are implemented to reflect hardware constraints. These limits act only during severe transients, leaving steady-state signals in the unsaturated domain where Lyapunov stability holds. Concurrently, an anti-windup scheme halts integration during saturation to safely prevent windup and restore unsaturated operation.

4.1 Simulation analysis

The simulation studies are conducted to investigate the performance of the MSTA-SMC under the predefined scenarios of levitation startup, dynamic speed tracking with sudden

reversals, and external disturbance rejection. These scenarios are designed to reflect the harsh working conditions of the motor, such as load torque variations and radial force perturbations. To ensure optimal performance, the control gains for each axis are carefully tuned, and the specific control parameters utilized in the simulation phase are summarized in Table 3.

Table 3: Controller gains for simulation.

Controller	Loop	Symbol	Value
PID Controller	Radial	K_P, T_I, T_D	1840, 20, 0.0167
	Speed	$K_{P\omega}$, $T_{I\omega}$	0.0132, 7.5
STA-SMC Controller	Radial	c_f, k_{1f}, k_{2f}	60, 25, 280
		η_{1f}, η_{2f}	0.6, 0.2
	Speed	λ_ω, $k_{1\omega}$, $k_{2\omega}$	100, 250, 8100
		$\eta_{1\omega}$, $\eta_{2\omega}$	0.6, 0.2
MSTA-SMC Controller	Radial	$L_b(s^{-1})$	100
		p_{b1}, p_{b2} $((m/s)^{1/2}, -)$	4, 0.4
		c_{b1}, c_{b2} $(s^{-1/2}, s^{-1})$	5, 15
	Speed	p_{m1}, p_{m2} $((rad/s)^{1/2}, -)$	4, 0.4
		c_{m1}, c_{m2} $(s^{-1/2}, s^{-1})$	20, 220

4.1.1 Suspension startup behavior

The first scenario evaluates the startup levitation performance from an initial radial offset of 1 mm in both the x- and y-directions. The levitation control loops are activated at t = 0.1 s. Figure 3 presents the radial displacement responses, whereas Figure 4 illustrates the corresponding control currents.

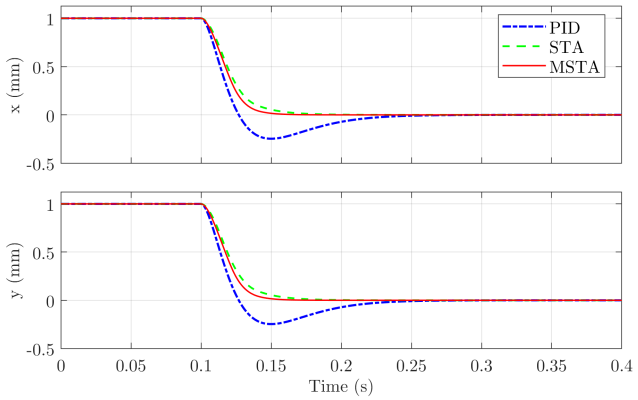


Figure 3: Simulated radial position during startup.

As observed in Figure 3, the PID controller suffers from a significant transient overshoot of approximately -0.25 mm before settling at t = 0.25 s. The standard STA successfully eliminates the transient overshoot. However, its convergence remains slow with a settling time of 0.1 s. In contrast, the proposed MSTA demonstrates superior transient performance. By leveraging linear proportional feedback, the MSTA accelerates the reaching phase, driving the rotor to the geometric origin without overshoot and achieving rapid convergence with a settling time of approximately 0.05 s.

As shown in Figure 4, all controllers initially command a

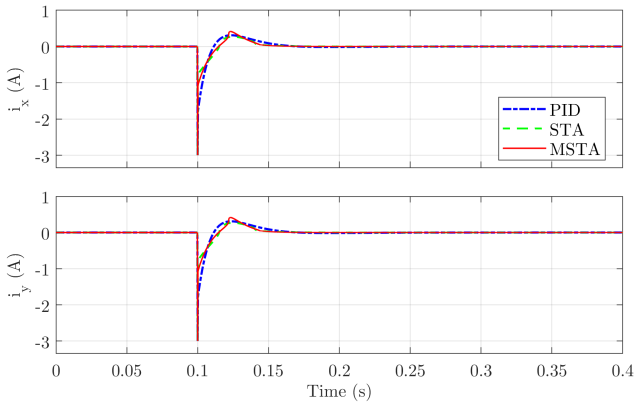


Figure 4: Simulated current during levitation startup.

saturated current of -3 A. The MSTA rapidly stabilizes at zero, providing a continuous control effort. The practical reduction of high-frequency chattering will be quantitatively verified in the experimental section.

4.1.2 Speed tracking and reversal

The second scenario examines the speed tracking performance of the rotational axis. The reference speed is first increased from 0 to 200 rad/s at t = 0.1 s and subsequently reversed to -200 rad/s at t = 1.0 s. The resulting speed trajectories and corresponding torque current responses are shown in Figure 5 and Figure 6, respectively.

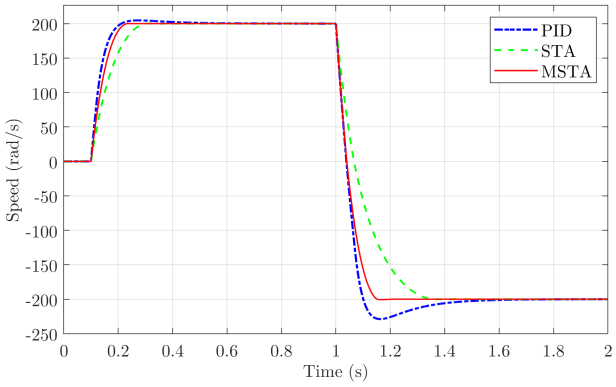


Figure 5: Simulated motor speed response.

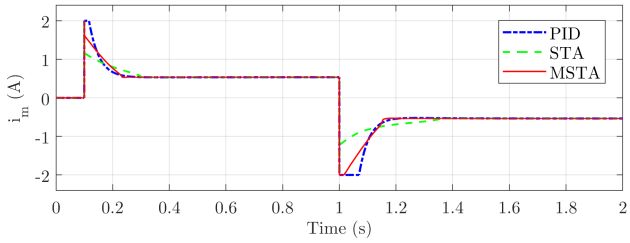


Figure 6: Simulated current during speed tracking.

Figure 5 shows that the PID controller experiences a minor overshoot during the initial acceleration phase and settles at approximately t = 0.4 s. More critically, during the severe speed reversal at t = 1.0 s, the linear controller suffers from a significant overshoot, dropping to approximately

-225 rad/s and requiring a recovery time of 0.5 s. The standard STA successfully eliminates the overshoot during both the acceleration and reversal phases. However, the standard STA exhibits an asymmetric and sluggish convergence rate. While it requires approximately 0.2 s to accelerate from 0 to 200 rad/s, its recovery during the severe speed reversal from 200 to -200 rad/s is notably slower, taking 0.35 s to reach the steady state. Conversely, the proposed MSTA demonstrates exceptional tracking precision and symmetric dynamics. It smoothly drives the motor to both target speeds without any transient overshoot, achieving a consistently fast settling time of about 0.15 s for both the initial startup and the reversal phases.

Figure 6 shows that the control currents reach the ±2 A limit to generate maximum torque. The MSTA recovers from saturation quickly, maintaining a stable current profile.

4.1.3 Robustness under disturbances

The final simulation scenario evaluates disturbance rejection. First, a sudden constant external force of 1 N is applied along both radial axes at t = 0.1 s to evaluate the disturbance rejection capability of the levitation subsystem. The transient displacement responses are illustrated in Figure 7, and the corresponding control currents are shown in Figure 8.

As observed in Figure 7, the external impact forces the rotor away from the magnetic center. The PID controller allows a maximum displacement of 0.38 mm and recovers slowly to the origin at t = 0.25 s. The standard STA improves the system robustness by limiting the peak displacement to 0.33 mm and forces a highly rapid recovery by t = 0.2 s. The MSTA further reduces the peak displacement to 0.28 mm, restoring the position steadily by t = 0.2 s.

Figure 8 shows that the rapid recovery of the STA requires a sharp current spike. The MSTA avoids this spike, providing a smoother current adjustment.

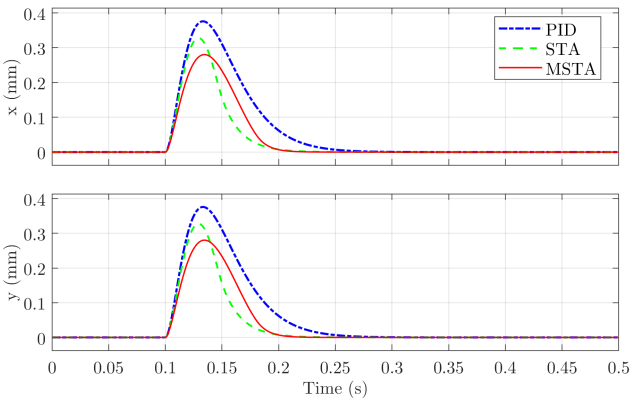


Figure 7: Simulated radial position under 1 N force.

The second robustness test examines the disturbance rejection capability of the rotational speed loop. A sudden load torque of 0.01 Nm is applied at t = 0.1 s while the motor operates at a constant speed of -200 rad/s. Figure 9 and Figure 10 display the speed recovery and the corresponding control current, respectively.

As shown in Figure 9, the sudden load causes a noticeable speed drop. The PID controller exhibits the weakest resistance, suffering a large 24.5 rad/s speed drop and requiring a prolonged period to recover by t = 0.9 s. The standard STA improves the dynamic stiffness by reducing the speed drop to 21 rad/s and forces an extremely rapid recovery by t = 0.35 s. However, the proposed MSTA exhibits the most enhanced robustness against load changes. It successfully limits the maximum speed drop to only 18 rad/s, outperforming both the linear baseline and the standard sliding mode controller, and steadily pulls the speed back to the reference value by t = 0.45 s.

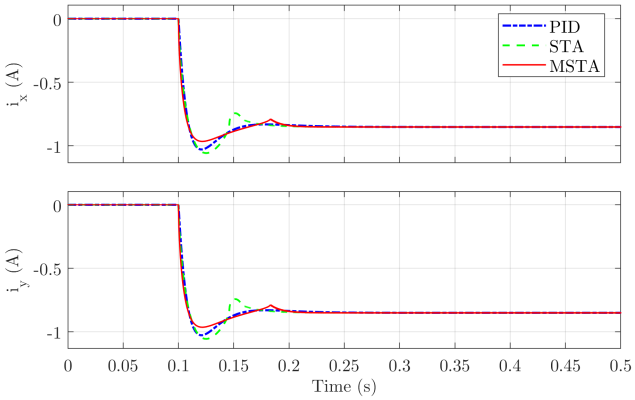


Figure 8: Simulated current under 1 N force.

To overcome this extra load, the control currents must settle at approximately -1.02 A. As illustrated in Figure 10, the aggressive speed recovery of the standard STA forces a sharp current overshoot to 1.08 A. Conversely, the MSTA minimizes the peak speed deviation while avoiding transient current overshoots, ensuring a much smoother transition and protecting the actuation hardware.

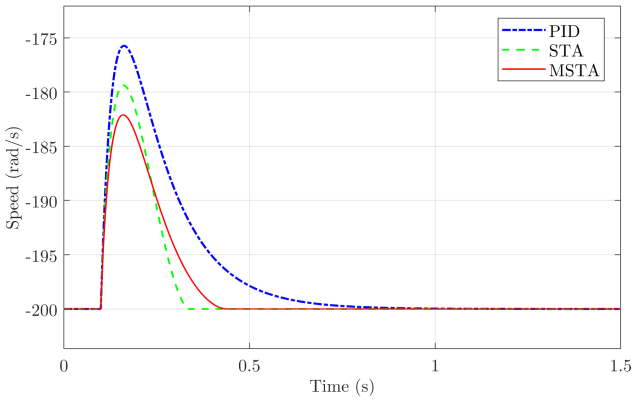


Figure 9: Simulated speed response with 0.01 N.m load.

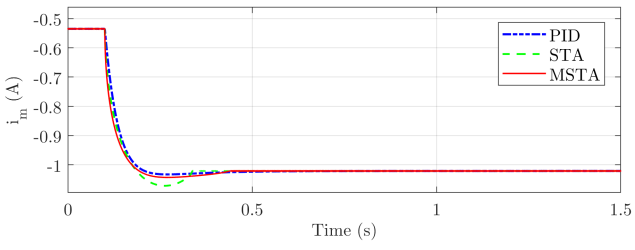


Figure 10: Simulated torque current under step load.

4.2 Experimental validation

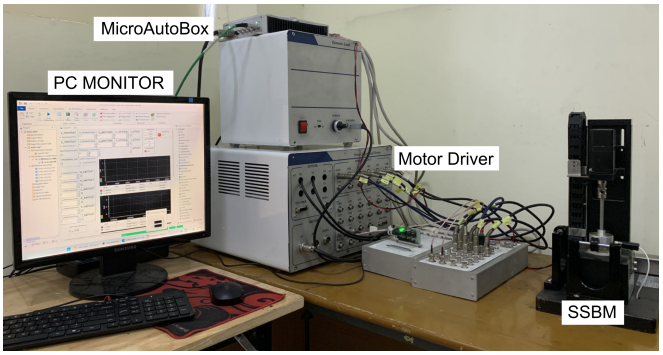


Figure 11: Experiment Setup.

Table 4: Controller gains for experiment.

Controller	Loop	Symbol	Value
PID Controller	Radial	$K_P,\ T_I,\ T_D$	1278, 16.67, 5
	Speed	$K_{P\omega},\ T_{I\omega}$	0.0088, 5
STA-SMC Controller	Radial	$c_f,\ k_{1f},\ k_{2f}$	60, 40, 50
		$\eta_{1f},\ \eta_{2f}$	0.6, 0.2
	Speed	$\lambda_\omega,\ k_{1\omega},\ k_{2\omega}$	100, 120, 70
		$\eta_{1\omega},\ \eta_{2\omega}$	0.6, 0.2
MSTA-SMC Controller	Radial	$L_b(s^{-1})$	60
		$p_{b1},\ p_{b2}$ $((m/s)^{1/2}, -)$	4, 0.4
		$c_{b1},\ c_{b2}$ $(s^{-1/2},\ s^{-1})$	5, 15
	Speed	$p_{m1},\ p_{m2}$ $((rad/s)^{1/2},\ -)$	8, 0.4
		$c_{m1},\ c_{m2}$ $(s^{-1/2},\ s^{-1})$	20, 50

To verify the practical performance of the proposed MSTA-SMC scheme, real-time hardware experiments are conducted on the laboratory test bench as shown in Figure 11. The control algorithms are developed in MATLAB/Simulink and executed on a dSPACE MicroAutoBox III real-time platform at a sampling frequency of 10 kHz. Parameter tuning and data logging are managed via dSPACE ControlDesk.

Rotor radial displacements are monitored using two VS-202-M eddy-current proximity sensors. Each sensor converts a measurement range of 0–2000 µm linearly into a 0–5 V analog output, which is digitized by the 16-bit ADC channels of the MicroAutoBox III. The rotational speed is acquired from a 2048-line/revolution relative encoder integrated into the Sigma-5 SGMJV load servo motor.

For actuation, the controller computes the desired phase currents and outputs the corresponding voltage commands via the DAC channels at a scaling of 1 V/A. These voltage signals are fed to a custom-designed 6-channel linear power amplifier operating in current-control mode with an internal closed-loop bandwidth of approximately 15 kHz. The amplifier internally regulates the phase currents according to the voltage references; so external current sensors are not required in the dSPACE control loop. Because this 15 kHz bandwidth is substantially higher than the dominant mechanical dynamics of the system, the current tracking dynamics can be neglected, and the controllers are implemented as single-loop schemes.

Consistent with the simulations, the hardware performance of the MSTA-SMC is validated against both the PID controller and the standard STA. The experimental control parameters are listed in Table 4.

During the hardware testing campaign, each operational scenario was repeated across multiple independent trials to verify closed-loop repeatability. Representative single-trial trajectories are presented rather than averaged curves to preserve the actual sensor noise and high-frequency switching ripple at 10 kHz, with transient settling times and peak deviations remaining consistent across all runs.

4.2.1 Experimental suspension startup

In the first hardware experiment, the rotor is initially displaced by 1 mm along both radial axes, with the levitation controllers activated at t = 0.2 s. The experimental transient displacements and the corresponding control currents are presented in Figure 12 and Figure 13, respectively.

Similar to the simulation results, Figure 12 illustrates that the PID controller exhibits a distinct transient overshoot, plunging to approximately -0.2 mm before settling at t = 0.35 s. In contrast, the displacement trajectories of both sliding mode controllers practically overlap, smoothly driving the rotor to the geometric origin without any overshoot and achieving a fast settling time of approximately 0.1 s.

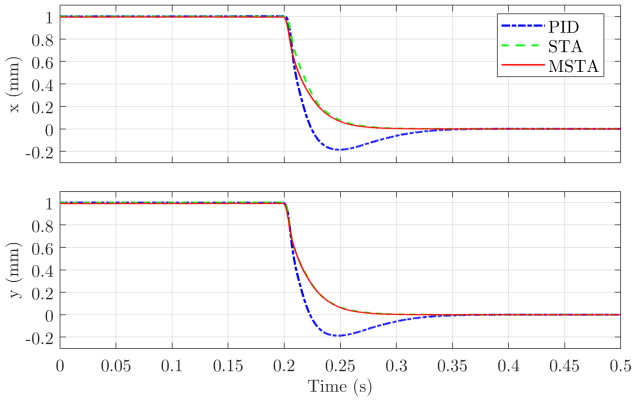


Figure 12: Measured radial position during startup.

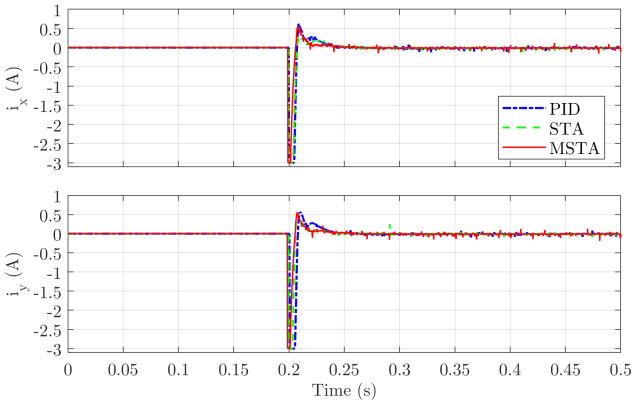


Figure 13: Control current during levitation startup.

To generate the initial restoring force, all controllers command a saturated current of -3 A. Upon exiting this saturation limit, the PID current exhibits severe ringing that

directly induces the mechanical overshoot. In contrast, both the standard STA and the proposed MSTA recover from saturation rapidly and efficiently, exhibiting highly similar transient current profiles before stabilizing near the zero level.

4.2.2 Experimental speed tracking

The second hardware scenario evaluates dynamic speed tracking, where the motor accelerates to 200 rad/s at t = 0.5 s and reverses to -200 rad/s at t = 3.5 s. The experimental speed and control current responses are presented in Figure 14 and Figure 15, respectively.

As shown in Figure 14, the PID controller experiences a significant overshoot to 260 rad/s, taking 1.7 s to settle. During the reversal phase, it suffers a significant overshoot to -350 rad/s, requiring 2.5 s to recover. The standard STA eliminates these overshoots but exhibits slower convergence, taking 0.6 s for startup and 1.3 s for reversal. Conversely, the MSTA achieves rapid and symmetric convergence, settling in only 0.5 s and 0.7 s, respectively.

This performance difference is explained by the control currents in Figure 15. The PID current stays saturated at -2 A for nearly 0.8 s during reversal, causing the large speed undershoot. The STA reduces its control effort early, delaying the speed recovery. The MSTA optimally maintains the required torque to accelerate the rotor, then efficiently exits saturation.

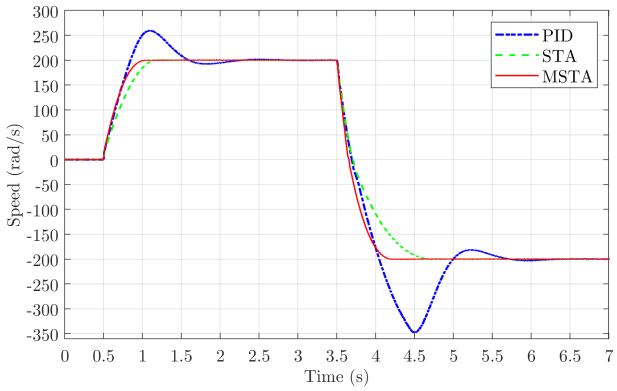


Figure 14: Measured motor speed response.

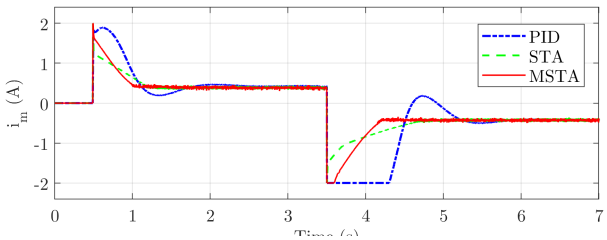


Figure 15: Control current during speed tracking.

4.2.3 Experimental disturbance rejection capability

The final hardware test evaluates disturbance rejection under physical external loads. First, to introduce a radial step force along the *x*- and *y*-axes, a 100 *g* standard mass is attached to the rotor shaft via an inelastic string routed horizontally over a pulley system. Under gravity, this mass produces a pulling

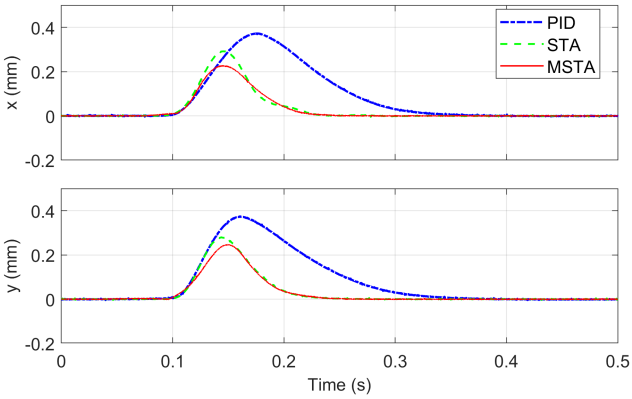


Figure 16: Measured radial position under 1 N force.

force of approximately 1 N as radial disturbance. Initially, the mass is held so that no tension acts on the levitated shaft. At $t = 0.1$ s, the mass is suddenly released to apply the horizontal step pulling force to the rotor. The transient displacement and the corresponding control current responses are presented in Figure 16 and Figure 17, respectively.

As shown in Figure 16, the PID controller exhibits limited disturbance rejection, allowing a maximum radial deviation of 0.38 mm and requiring 0.3 s to recover. The standard STA improves the dynamic stiffness by limiting the peak displacement to 0.29 mm and forces an extremely rapid recovery, settling at $t = 0.22$ s. However, the proposed MSTA demonstrates the most superior robustness against radial impacts. It successfully restricts the maximum displacement to only 0.25 mm and effectively restores the levitation position alongside the standard STA by t = 0.23 s.

To compensate for the 1 N force, the control currents must settle at approximately -0.8 A. As shown in Figure 17, the rapid recovery of the standard STA causes a sharp current spike to nearly -1.1 A. Conversely, the MSTA minimizes the peak displacement while maintaining a much smoother current transition. By avoiding this severe spike, the MSTA ensures robust disturbance rejection with an optimized control effort.

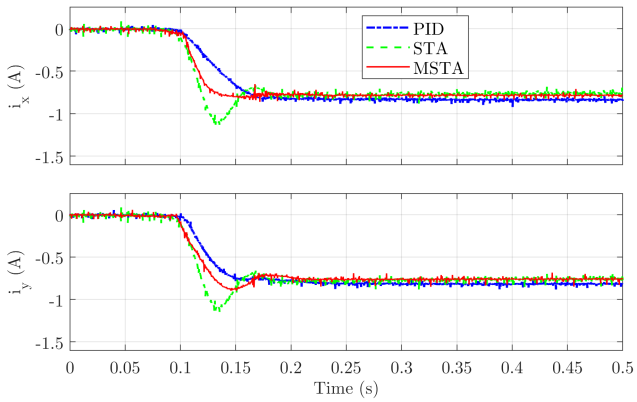


Figure 17: Control current under 1 N force.

Furthermore, a 0.01 N·m load torque is introduced at t = 0.5 s while the motor operates at -200 rad/s. This opposing torque is generated by the coupled load servo motor in torque control mode, controlled by a voltage command from the controller to the load driver. To clearly visualize the transient dynamics and the high-frequency measurement noise, Figure

Table 5: Quantitative performance and chattering comparison.

Scenario	Metric	PID	STA	MSTA
Startup levitation	Settling time t_s(s)	0.35	0.10	0.10
(1 mm initial offset)	Overshoot (mm)	-0.20	0.00	0.00
Speed Acceleration & Reversal	Startup settling time t_s (s)	1.70	0.60	0.50
(0 to 200 to -200 rad/s)	Reversal recovery time (s)	2.50	1.30	0.70
	Reversal peak speed (rad/s)	-350	-200	-200
Radial Force Disturbance	Peak displacement deviation (mm)	0.38	0.29	0.25
(1 N step force)	Recovery time (s)	0.30	0.22	0.23
	Current spike / overshoot (A)	-1.02	-1.10	-0.80
Load Torque Disturbance	Maximum speed drop (rad/s)	20.0	17.0	14.0
(0.01 N·m step torque)	Recovery time (s)	1.80	1.30	1.50
Actuation Chattering	Total Variation TV (A)	12.1084	99.4972	79.8940
(Steady-state from $t = 6.0$ s to 7.0 s of experiment 4.2.2)	Current Ripple RMS (A)	0.00550	0.02500	0.02002

18 and Figure 19 display the experimental speed recovery and the corresponding control current in separated subplots, respectively.

Figure 18 demonstrates that the applied load disturbance produces an immediate reduction in speed for all controllers. Under PID control, the motor experiences a severe speed deviation of approximately 20 rad/s. During the recovery phase, the motor speed exhibits an oscillation before finally settling at around t =1.8 s. The standard STA improves the dynamic stiffness marginally, reaching a 17 rad/s peak deviation and eliminating the secondary oscillation to settle at t = 1.3 s. In contrast, the MSTA exhibits the most robust disturbance rejection, limiting the maximum speed drop to only 14 rad/s and achieving accurate, monotonic convergence at t = 1.5 s without any prolonged oscillations.

The control current responses in Figure 19 explain this behavior. The PID current responds slowly, which directly induces the massive speed deviation. While both sliding mode controllers react swiftly to compensate for the sustained mechanical load, the aggressive speed recovery of the standard STA forces a sharp current transient, plunging to a spike of nearly -0.9 A. Conversely, the MSTA adjusts its current efficiently and optimally. It smoothly reaches a steady state of -0.8 A without excessive peaking. This confirms its practical capability to reject load variations and minimize peak speed deviations.

To provide an objective assessment across all tested scenarios, the quantitative performance metrics and chattering indices of the three controllers are summarized in Table 5. The evaluation encompasses transient settling times, peak deviations under disturbances, and steady-state chattering metrics computed between 6.0 s and 7.0 s. Specifically, the total variation of the control current is defined as $TV = \sum_{k=1}^{N-1} |i(k+1) - i(k)|$, where N represents the sample count. As indicated in Table 5, the proposed MSTA-SMC achieves the fastest dynamic recovery and smallest tracking deviations while effectively suppressing current chattering.

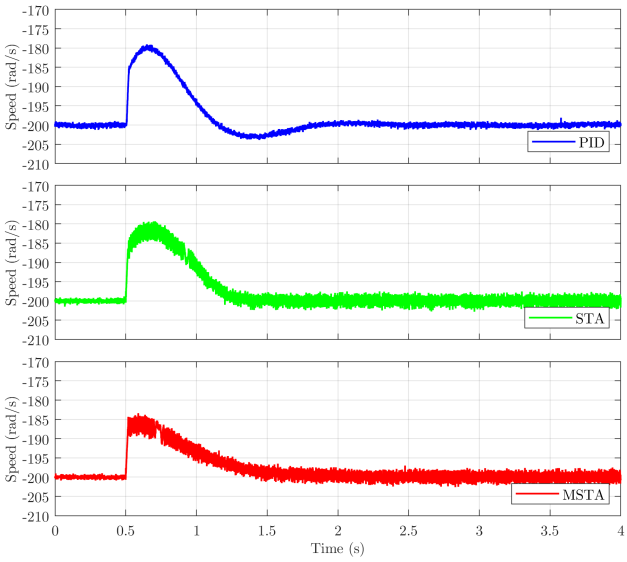


Figure 18: Measured speed response with 0.01 Nm load.

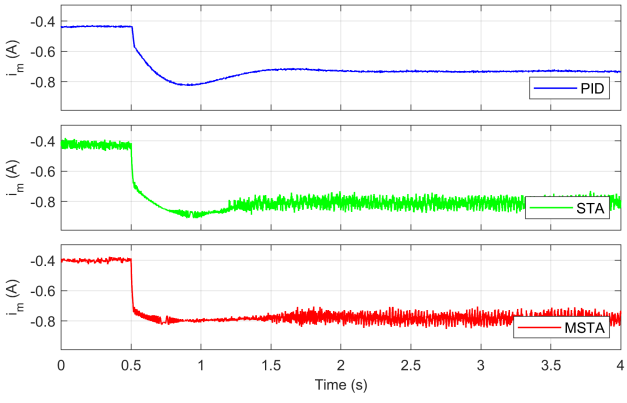


Figure 19: Control torque current under step load.

5. Conclusion

This study developed a robust MSTA-SMC framework for an SSBM to reduce dynamic disturbances in both the translation and rotation loops. The mathematical modeling, rigorous Lyapunov stability analysis, numerical simulations, and real-time hardware experiments were conducted to verify the feasibility and real-time performance of the developed control scheme. Evaluated against both a conventional PID controller and the standard STA, the MSTA-SMC demonstrated superior dynamic stiffness and enhanced convergence speed. It effectively mitigated transient overshoots, significantly reduced speed reversal recovery times, and suppressed actuation chattering by approximately 20% compared to the standard STA, making it highly suitable for reliable hardware operation.

Although the reaching law guarantees finite-time convergence to the sliding manifolds, the radial position tracking errors converge asymptotically as a consequence of using linear sliding surfaces. Consequently, future work will integrate nonlinear terminal sliding manifolds for the translational axes to achieve full finite-time position error convergence. Additionally, future efforts will explore finite-time disturbance estimation techniques, adaptive control laws, and the detailed analytical treatment of input saturation constraints, thereby bypassing the requirement of predefined disturbance upper bounds, which will enhance the motor's resilience against complex, time-dependent perturbations.

Acknowledgement

This research is funded by Hanoi University of Science and Technology (HUST) under project number T2024-TĐ-007.

References

[1] Liu B (2015) *Survey of bearingless motor technologies and applications*. 2015 IEEE International Conference on Mechatronics and Automation (ICMA), Beijing, China, pp. 1983-1988

[2] Osa M, Masuzawa T, Orihara R, Tatsumi E (2017) *Compact maglev motor with full DOF active control for miniaturized rotary blood pumps*. 2017 11th International Symposium on Linear Drives for Industry Applications (LDIA), Osaka, Japan, pp. 1-6

[3] Li W, Chau KT, Ching TW, Wang Y, Chen M (2015) *Design of a High-Speed Superconducting Bearingless Machine for Flywheel Energy Storage Systems.* IEEE Transactions on Applied Superconductivity, vol. 25, no. 3, pp. 1-4

[4] Humza M, Noh S, Jeong HS, Yazdan T, Doukhi O, Cho HW (2024) *A Novel Design of Modular Bearingless PMSM Motor for Ultra Clean Applications*. IEEE Access, vol. 12, pp. 21576-21585

[5] Stephens LS, Kim DG (2002) *Analysis and simulation of a Lorentz-type slotless, self-bearing motor*. Control Engineering Practice, vol. 10, no. 8, pp. 899-905

[6] Baumgartner T, Burkart RM, Kolar JW (2014) *Analysis and Design of a 300-W 500 000-r/min Slotless Self-Bearing Permanent-Magnet Motor*. IEEE Transactions on Industrial Electronics, vol. 61, no. 8, pp. 4326-4336

[7] Borque Gallego G, Rossini L, Achtnich T, Araujo DM, Perriard Y (2021) *Efficiency Optimization of Slotless Magnetic-Bearing Machines*. IEEE Transactions on Industry Applications, vol. 57, no. 6, pp. 6833-6843

[8] Nguyen QD, Ueno S (2011) *Modeling and Control of Salient-Pole Permanent Magnet Axial-Gap Self-Bearing Motor*. IEEE/ASME Transactions on Mechatronics, vol. 16, no. 3, pp. 518-526

[9] Nguyen HP, Nguyen XB, Bui TT, Ueno S, Nguyen QD (2019) *Analysis and Control of Slotless Self-Bearing Motor*. Actuators, vol. 8, no. 3, 57

[10] Nguyen QD, Nguyen HP, Nguyen KT, Vo DN, Nguyen XB, Ueno S, Giap VN (2023) *Robust Sliding Mode Control for Slotless-Self Bearing Motor System*. Journal of Electrical Engineering & Technology, vol. 18, no. 3, pp. 1893-1907

[11] Gambhire SJ, Kishore DR, Londhe PS, Pawar SN (2021) *Review of sliding mode based control techniques for control system applications*. International Journal of dynamics and control, vol. 9, no. 1, pp. 363-378

[12] Guldner J, Utkin V (2000) *The chattering problem in sliding mode systems*. Proc. 14th Int. Symp. of Mathematical Theory of Networks and Systems (MTNS)

[13] Ngo HK, Giap VN, Nguyen QD (2026) *Super-twisting sliding mode control for slotless self bearing motor under disturbance effects of position and rotation axes*. Results in Engineering, vol. 30, 111009

[14] Liu YC, Laghrouche S, Depernet D, N'Diaye A, Djerdir A, Cirrincione M (2024) *Disturbance-observer-based speed control for SPMSM drives using modified super-twisting algorithm and extended state observer*. Asian Journal of Control, vol. 26, no. 3, pp. 1089-1102